applied sciences

MDPI

Article

A Level-Set-Based Density Method for Buckling Optimization of Structure with Curved Grid Stiffeners

Yifan Zhang, Ye Tian and Qi Xia *

State Key Laboratory of Intelligent Manufacturing Equipment and Technology, School of Mechanical Science and Engineering, Huazhong University of Science and Technology, Wuhan 430074, China; z_yifan0829@hust.edu.cn (Y.Z.); tianye@mail.hust.edu.cn (Y.T.)
* Correspondence: qxia@mail.hust.edu.cn

Abstract: Curved grid stiffeners, compared to straight stiffeners, offer greater flexibility in adjusting the force transmission paths and give better structural performance. In this paper, a level-set-based density method is employed to generate layouts of curved grid stiffeners so that the critical buckling load factor (BLF) of the stiffened structures is improved. During the optimization process, volume constraint is incorporated to control material utilization, and gradient constraints are employed to maintain uniformity in the width of the stiffeners. Finally, the proposed method is demonstrated through several numerical examples.

Keywords: structural optimization; grid stiffener; level set method; buckling load optimization

check for updates

Citation: Zhang, Y.; Tian, Y.; Xia, Q. A Level-Set-Based Density Method for Buckling Optimization of Structure with Curved Grid Stiffeners. *Appl. Sci.* **2024**, *14*, 5695. https://doi.org/10.3390/app14135695

Academic Editor: Giovanni Bernardini

Received: 23 May 2024
Revised: 26 June 2024
Accepted: 27 June 2024
Published: 29 June 2024

1. Introduction

Stiffeners can effectively enhance structures in bending stiffness, strength. Therefore, they have been widely utilized in aerospace, automotive, architectural, and other fields [1–3]. Curved grid stiffeners typically consist of many curved and crossed ribs, and they can adjust the load paths according to the different requirements of different local regions of the structure. Therefore, they have greater potential in reducing structural weight and improving structural performance [4–10], and there has been growing interests in the layout optimization of curved grid stiffeners [6,8,11–15].

The stability of a structure is an important indicator of its performance. When subjected to axial compression and the load reaches a certain value, structures often experience buckling failure [16]. Therefore, the buckling performance of structures becomes a key factor in design and optimization. In related studies, Cai et al. [17] employed generalized beam theory to analyze buckling in thin-walled structures. Ferrari et al. [18] presented a topology optimization of structures under plane stress condition for linear buckling with 250 lines of code. Xu and others [19] presented an innovative linear interpolation approach to improve the buckling resistance of structures in topology optimization. In related experimental research of buckling response, Falkowicz [20] performed both linear and nonlinear buckling analyses, as well as experimental tests, on a thin-walled composite plate with a central cutout under axial compression. In latest developments [21,22], asymmetric systems and their mechanical couplings have been utilized to create elements that can function as elastic components, and comprehensive experimental and numerical studies have been conducted using multiple detection techniques and interdisciplinary approaches.

For stiffened structures, the introduction of stiffeners significantly improves the buckling resistance. In addition, optimizing the layout of stiffeners can further amplify this advantage [4,7,8,23]. The design optimization of stiffened structures considering buckling characteristic has become an important research topic. Kapania et al. [4] optimized stiffened plates primarily governed by buckling phenomena and demonstrated that, compared to straight stiffeners, curved stiffeners provide enhanced design space, resulting in better design outcomes. A buckling analysis of composite plates was proposed [8],

indicating that arranging curved stiffeners for composite plates can improve buckling load compared to straight stiffeners. Shi and co-workers [24] explored the static, vibration, and buckling behaviors of stiffened plates under in-plane compressive and tensile stresses. Hao et al. [25] and Wang et al. [26] utilized the smeared stiffener method (SSM) and the Rayleigh–Ritz method to forecast and determine the buckling load of hierarchical stiffened plates. Paschero and Hyer [5] significantly improved the buckling performance for elliptical lattice cylinders by adjusting the distribution of circumferential stiffeners. An effective optimization strategy for cylindrical structure with reinforced cutouts was proposed by Hao et al. [7], employing curved stiffeners to enhance the load distribution and local stiffness of cylindrical stiffened shells. Luo et al. [27] proposed an approach for optimizing the arrangement of stiffeners in slender structure, considering the maximum critical buckling load under geometric uncertainties that vary spatially. Wang et al. [13,28] calculated the global and local buckling loads of periodically grid-stiffened composite plates and shells and optimized the layout of curved stiffeners. A data-driven optimization approach was presented to maximize the critical BLF [29]. These research works on the design optimization considering buckling of stiffened structures further promote the progress and development of structural optimization, especially in the field of structures with curved stiffeners.

Theoretically, structures have many linear buckling modes linked to relevant critical load values. But in engineering applications, the smallest critical load value, namely, the critical buckling load factor (BLF), is under consideration, as exceeding this load leads to structural instability and failure. Therefore, in optimization, it is essential to maximize the critical BLF of the structure to enhance its stability [16,28,30,31]. However, it should also be considered that in practice, structural instability often occurs before reaching the critical buckling load. This is due to the potential presence of imperfections in the structure or the material reaching its yield point.

In this paper, a level-set-based density method proposed in our previous study [15] is used to optimize the critical BLF of structures with curved grid stiffeners. This provides new insights for the buckling research of stiffened structures. Two level set functions are converted by cosine function, combined using the maximum function, and projected to real densities using an approximate Heaviside function. The Mindlin plate theory is employed for finite element analysis of buckling. After that, the sensitivity analysis is performed, and the design variables are updated. Ultimately, the optimized results are obtained. The effectiveness of this approach in enhancing structural stability is proven by several numerical examples.

The main structure of the paper is outlined as follows. Section 2 presents the definition of the grid stiffener structure. Section 3 discusses the relevant constraints for stiffener optimization. The optimization framework and sensitivity analysis are detailed in Section 4. Several numerical examples and result analyses are presented in Section 5. Section 6 gives the conclusions.

2. Representation of Grid-Stiffener Model

2.1. Definition of Stiffener Height

The total height h_e at the center of the e-th element of the grid-stiffened structure is obtained by adding the base height h_b and the stiffener height h_s. h_e is calculated from the function $h(\boldsymbol{x})$ at the element center $\boldsymbol{x}_e = (x_e, y_e)$, and $h(\boldsymbol{x})$ is given by

$$h(\boldsymbol{x}) = h_b + \tilde{\rho}(\boldsymbol{x}) h_s \tag{1}$$

where $\tilde{\rho}(\boldsymbol{x})$ is regarded as the real density of stiffeners, describing their layout. When $\tilde{\rho}(\boldsymbol{x})$ is 1, it is considered as stiffeners being present, while values close to 0 indicate the absence of stiffeners.

The real density $\tilde{\rho}(\boldsymbol{x})$ is derived through a threshold projection of the function $\rho(\boldsymbol{x})$. The threshold projection employed in this paper is an approximate Heaviside function [32]

$$\tilde{\rho}(\boldsymbol{x}) = \frac{\tanh(\tau\eta) + \tanh[\tau(\rho(\boldsymbol{x}) - \eta)]}{\tanh(\tau\eta) + \tanh[\tau(1 - \eta)]} \tag{2}$$

where the value of parameter τ affects the approximation of Equation (2) to the ideal Heaviside function; η controls the location of the step point of the function. As shown in Figure 1, as τ increases, this function approaches the ideal Heaviside function more closely. In this paper, τ is set to 7. In addition, as depicted in Figure 1, when $\eta = 0.5$, the Step Point 1 is positioned at $x = 0.5$. When $\eta = 0.8$, Step Point 2 of the approximate Heaviside function is located at $x = 0.8$. Moreover, this parameter is related to the width of the stiffeners, as discussed later, and can be treated as a design variable in the optimization.

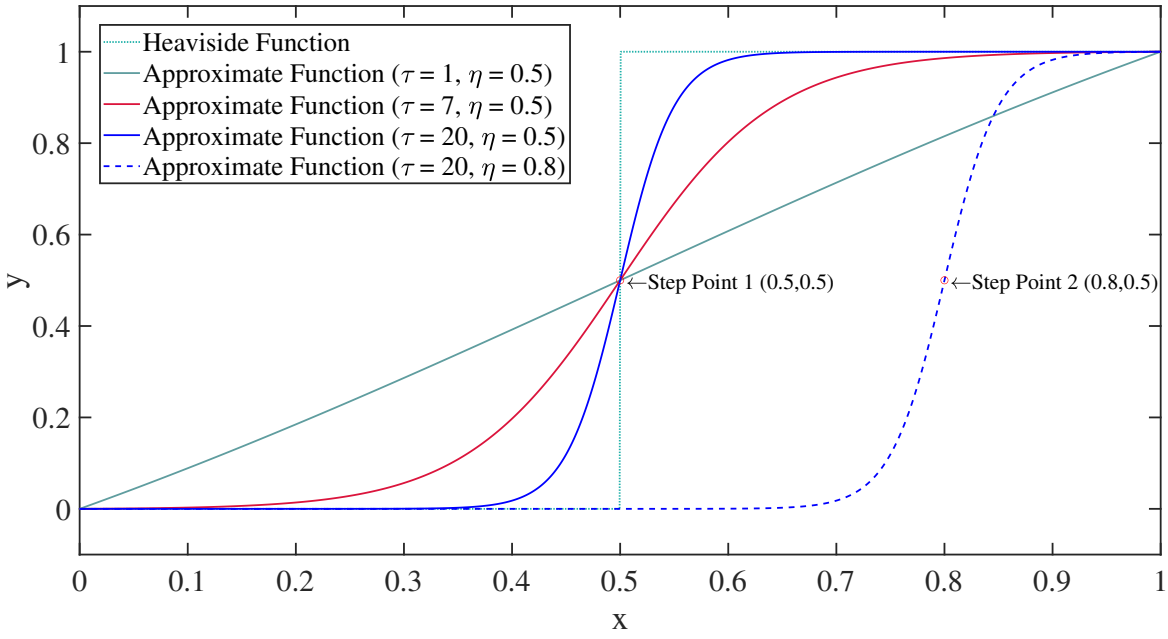

Figure 1. The effect of parameters τ and η on the approximate Heaviside function.

The function $\rho(\boldsymbol{x})$ is obtained by taking the maximum value from two functions, $\Gamma(\boldsymbol{x})$ and $\Theta(\boldsymbol{x})$, i.e.,

$$\rho(\boldsymbol{x}) = \max\{\Gamma(\boldsymbol{x}), \Theta(\boldsymbol{x})\} \tag{3}$$

where the function $\max\{\cdot, \cdot\}$ is described as [15]

$$\max\{s, t\} = \frac{1}{2}[s + t + \text{abs}_\varepsilon(s - t)] \tag{4}$$

where $\text{abs}_\varepsilon(a) = \sqrt{a^2 + \varepsilon}$; and ε is set to 0.01. The functions $\Gamma(\boldsymbol{x})$ and $\Theta(\boldsymbol{x})$ are derived from two functions $\gamma(\boldsymbol{x})$ and $\theta(\boldsymbol{x})$ through cosine transformations [33], i.e.,

$$\Gamma(\boldsymbol{x}) = \frac{1}{2} + \frac{1}{2}\cos\left(\frac{2\pi}{\mu_1}\gamma(\boldsymbol{x})\right) \tag{5}$$

$$\Theta(\boldsymbol{x}) = \frac{1}{2} + \frac{1}{2}\cos\left(\frac{2\pi}{\mu_2}\theta(\boldsymbol{x})\right) \tag{6}$$

where $\gamma(\boldsymbol{x})$ and $\theta(\boldsymbol{x})$ represent fundamental level set functions; μ_1 and μ_2 correspond to the wavelengths of two cosine functions. It can be easily observed that the ranges of the functions $\Gamma(\boldsymbol{x})$ and $\Theta(\boldsymbol{x})$ are both between 0 and 1. When τ in Equation (2) is sufficiently

large and the norms of gradient vector of the fundamental level set functions $\gamma(\boldsymbol{x})$ and $\theta(\boldsymbol{x})$ equal 1, the width w_s of the stiffeners can be expressed as [15]

$$w_s = \frac{\mu}{\pi} \arccos(2\eta - 1) \tag{7}$$

where μ can be μ_1 or μ_2. From Equation (7), it can be observed that the width w_s varies in proportion to the wavelength μ of the cosine functions, and there is a relationship between the parameters w_s and η. Therefore, η can be used as a design variable to change the width of the stiffeners.

Based on the aforementioned theories, an example process for generating grid stiffeners is provided. Figure 2 shows the images of the fundamental level set functions $\gamma(\boldsymbol{x})$ and $\theta(\boldsymbol{x})$. And Figure 3 shows their corresponding contours. It can be observed that the contours of the level set functions are at 0° and 90°. The colors transition from blue to green from bottom to top, indicating a gradual change from smaller to larger values in Figures 2 and 4.

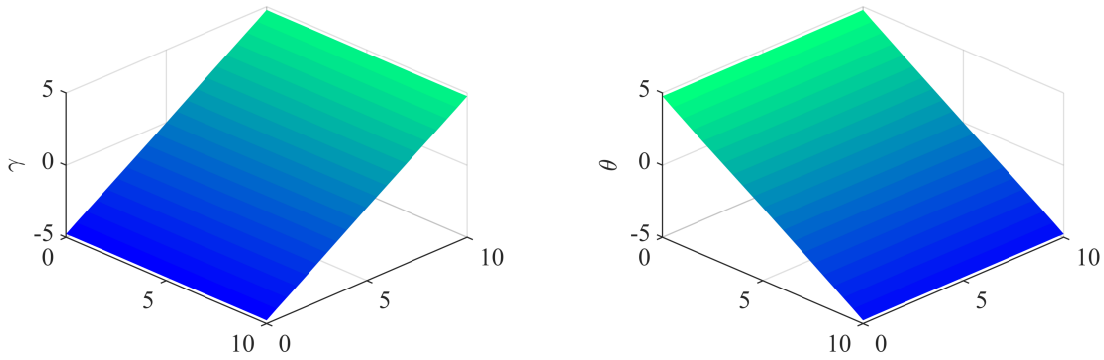

(**a**) $\gamma(\boldsymbol{x})$ (**b**) $\theta(\boldsymbol{x})$

Figure 2. Examples of the fundamental level set functions $\gamma(\boldsymbol{x})$ and $\theta(\boldsymbol{x})$.

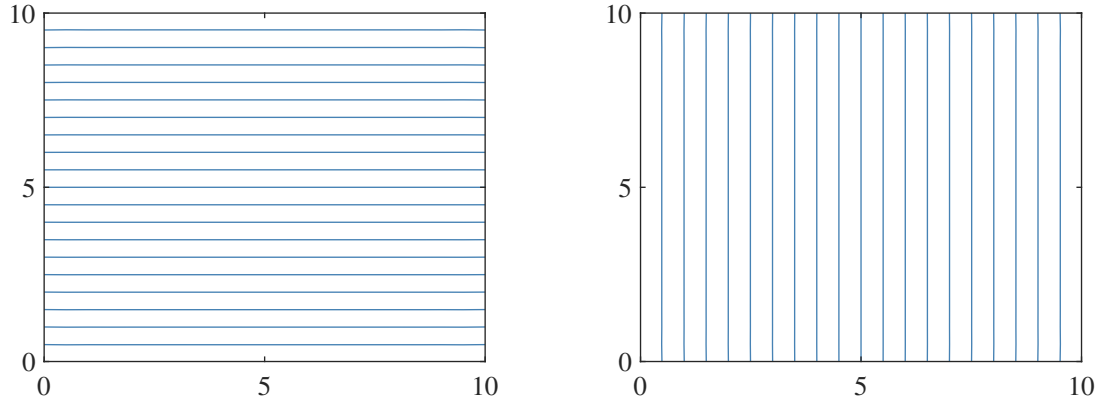

(**a**) contour lines of $\gamma(\boldsymbol{x})$ (**b**) contour lines of $\theta(\boldsymbol{x})$

Figure 3. Contour lines of the level set functions.

Figure 4 shows the images of functions $\Gamma(\boldsymbol{x})$ and $\Theta(\boldsymbol{x})$, which are obtained by applying the cosine transformation in Equations (5) and (6) to the level set functions $\gamma(\boldsymbol{x})$ and $\theta(\boldsymbol{x})$, respectively. When projected onto a horizontal plane, it contains width information. The grayscale images of $\Gamma(\boldsymbol{x})$ and $\Theta(\boldsymbol{x})$ are shown in Figure 5.

After applying the maximum combination from Equations (3) and (4), Figure 6a is obtained. Subsequently, the threshold projection in Equation (2) is used to generate the final real density distribution map, as seen in Figure 6b. It can be observed that the threshold projection effectively reduces the amount of intermediate density, making the grid stiffener structure clearer and more visually intuitive.

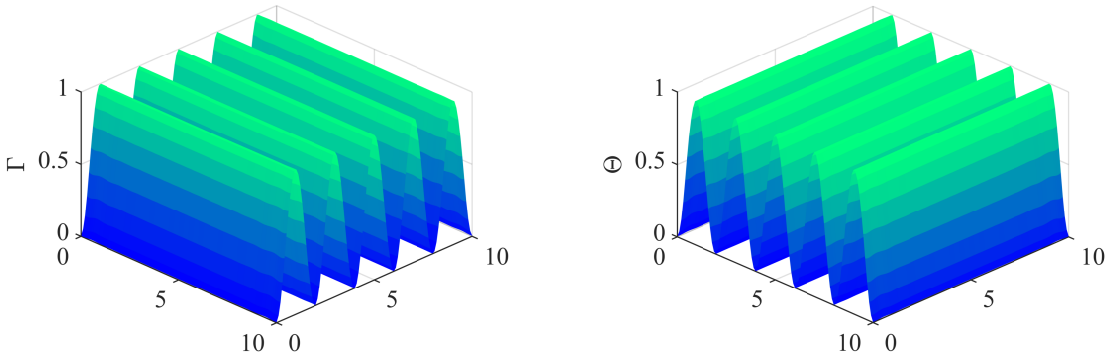

(**a**) $\Gamma(\boldsymbol{x})$ (**b**) $\Theta(\boldsymbol{x})$

Figure 4. The functions after the cosine transformation.

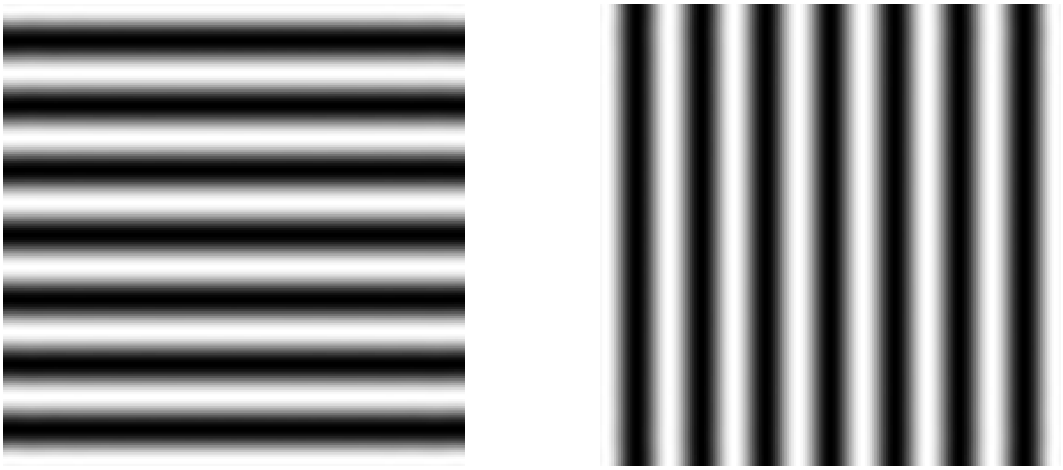

(**a**) $\Gamma(\boldsymbol{x})$ (**b**) $\Theta(\boldsymbol{x})$

Figure 5. The grayscale images of functions $\Gamma(\boldsymbol{x})$ and $\Theta(\boldsymbol{x})$.

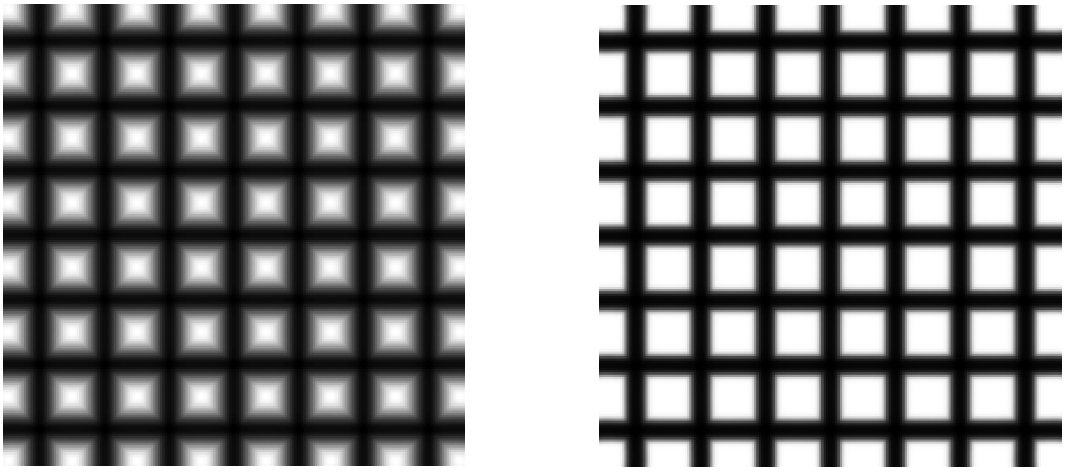

(**a**) $\rho(\boldsymbol{x})$ (**b**) $\tilde{\rho}(\boldsymbol{x})$

Figure 6. The images of the function after maximization combination and threshold projection.

2.2. Fundamental Level Set Function Based on RBFs

The radial basis functions (RBFs) [34–38] are utilized here to construct the fundamental level set functions $\gamma(\boldsymbol{x})$ and $\theta(\boldsymbol{x})$, i.e.,

$$\gamma(\boldsymbol{x}) = \sum_{i=1}^{m} \alpha_i \varphi(\boldsymbol{x}, \boldsymbol{q}_i) \tag{8}$$

$$\theta(\boldsymbol{x}) = \sum_{i=1}^{m} \beta_i \varphi(\boldsymbol{x}, \boldsymbol{q}_i) \tag{9}$$

where α_i and β_i represent the coefficients of the i-th RBF; $\boldsymbol{q}_i$ is the knot of the i-th RBF; m stands for the total number of RBFs. The RBF at knot $\boldsymbol{q}_i$ is denoted as

$$\varphi(\boldsymbol{x}, \boldsymbol{q}_i) = \varphi(\|\boldsymbol{x} - \boldsymbol{q}_i\|) \tag{10}$$

where the $\|\cdot\|$ represents the Euclidean norm.

In this study, the compactly supported RBF (CS-RBF) with C^2 continuity is utilized. It is expressed as [37]

$$\varphi(t) = (1-t)_+^4 (4t+1) \tag{11}$$

where $(\cdot)_+$ represents $\max\{\cdot, 0\}$; t is formulated as

$$t(\boldsymbol{x}, \boldsymbol{q}_i) = \frac{1}{d_s} \sqrt{\|\boldsymbol{x} - \boldsymbol{q}_i\|^2 + \kappa^2} \tag{12}$$

where d_s is the support radius of CS-RBF; κ is set as 10^{-4} to prevent division by zero.

3. Constraints of Stiffeners

3.1. Constraint of Volume

In order to ensure that the optimization meets practical volume or mass requirements, material volume constraint for stiffeners is defined as

$$V = \sum_{e=1}^{n} \tilde{\rho}(\boldsymbol{x}_e) h_s A_e \leq \overline{V} \tag{13}$$

where V denotes the total volume of stiffeners; h_s is the thickness of stiffener; A_e denotes the area of the e-th element; and $\overline{V}$ stands for the maximum allowable volume of stiffeners.

3.2. Constraint of Uniform Width

The uniformity of stiffener width holds substantial significance for practical engineering manufacturing because in some applications, stiffeners with uniform widths are easier to manufacture. One effective approach to achieve this goal is to ensure that the norm of the gradient vector of the fundamental level set functions is equal to 1 across nearly all points. The norm of the gradient vector of $\gamma(\boldsymbol{x})$ is provided by

$$\|\nabla\gamma(\boldsymbol{x})\| = \sqrt{\left(\sum_{i=1}^{m} \alpha_i \frac{\partial \varphi}{\partial x}(\boldsymbol{x}, \boldsymbol{q}_i)\right)^2 + \left(\sum_{i=1}^{m} \alpha_i \frac{\partial \varphi}{\partial y}(\boldsymbol{x}, \boldsymbol{q}_i)\right)^2} \tag{14}$$

where $\partial\varphi/\partial x$ and $\partial\varphi/\partial y$ are, respectively, the partial derivatives of φ with respect to x and y. According to Equation (11), they are defined as [37]

$$\frac{\partial \varphi}{\partial x}(\boldsymbol{x}, \boldsymbol{q}_i) = -20 \cdot t(\boldsymbol{x}, \boldsymbol{q}_i) \cdot (1 - t(\boldsymbol{x}, \boldsymbol{q}_i))_+^3 \frac{\partial t}{\partial x}(\boldsymbol{x}, \boldsymbol{q}_i) \tag{15}$$

$$\frac{\partial \varphi}{\partial y}(\boldsymbol{x}, \boldsymbol{q}_i) = -20 \cdot t(\boldsymbol{x}, \boldsymbol{q}_i) \cdot (1 - t(\boldsymbol{x}, \boldsymbol{q}_i))_+^3 \frac{\partial t}{\partial y}(\boldsymbol{x}, \boldsymbol{q}_i) \tag{16}$$

The $\|\nabla\theta(\boldsymbol{x})\|$ of the function $\theta(\boldsymbol{x})$ can be obtained similarly.

The subsequent two constraints can ensure that at the center point $\boldsymbol{x}_e$ of each element, $\|\nabla\gamma(\boldsymbol{x}_e)\|$ and $\|\nabla\theta(\boldsymbol{x}_e)\|$ are close to 1. Let d_e^{ϕ} and d_e^{ψ} denote the constraints of the e-th element on $\gamma(\boldsymbol{x})$ and $\theta(\boldsymbol{x})$. Following the methods in [39–41], equality constraints can be transformed into inequality constraints as

$$d_e^{\gamma} = \left(\|\nabla\gamma(\boldsymbol{x}_e)\| - 1\right)^2 \leq \xi, \quad e = 1 \ldots n \tag{17}$$

$$d_e^{\theta} = \left(\|\nabla\theta(\boldsymbol{x}_e)\| - 1\right)^2 \leq \xi, \quad e = 1 \ldots n \tag{18}$$

The p-norm approach [42] is utilized to consolidate the constraints as

$$g_{\gamma} = \left(\sum_{e=1}^{n} \left(d_e^{\gamma}\right)^{p_2}\right)^{1/p_2} \leq \xi \tag{19}$$

$$g_{\theta} = \left(\sum_{e=1}^{n} \left(d_e^{\theta}\right)^{p_2}\right)^{1/p_2} \leq \xi \tag{20}$$

where ξ is the upper limit of the two constraints; n is the amount of finite elements; and $p_2 > 0$ is the parameter of the p-norm.

4. Optimization Framework and Sensitivity Analysis

4.1. Definition of Buckling Load Optimization Problem

The buckling optimization problem is defined as

$$\begin{aligned} \min_{\alpha_i, \beta_i, \eta} \quad & J = -\lambda_1 \\ \text{s.t.} \quad & (\mathbf{K} - \lambda_1 \mathbf{G})\boldsymbol{\varphi}_1 = 0 \\ & \delta_{\min} \leq \alpha_i, \beta_i \leq \delta_{\max} \\ & \eta_{\min} \leq \eta \leq \eta_{\max} \\ & V \leq \overline{V} \\ & g_{\gamma}, g_{\theta} \leq \xi \end{aligned} \tag{21}$$

where λ_1 represents the fundamental BLF; $\boldsymbol{\varphi}_1$ denotes the eigenvector corresponding to the eigenvalue λ_1; $\mathbf{K}$ stands for the global stiffness matrix, while $\mathbf{G}$ represents the global geometric stiffness matrix; $\delta_{\min}$ and $\delta_{\max}$, respectively, stand for the lower and upper limits of the design variables α_i and β_i; $\eta_{\min}$ and $\eta_{\max}$ indicate the minimum and maximum values of the design parameter η; g_{γ} and g_{θ} are the gradient constraint functions for the two fundamental level set functions, and ξ represents the maximum value of the gradient constraints; V denotes the total volume of stiffeners, while $\overline{V}$ indicates the volume constraint of stiffeners.

4.2. Finite Element Analysis

The Mindlin plate theory [43–46] is used in the finite element analysis. Additionally, we assumed the substrate and stiffeners are made of the same material. Therefore, the stiffness matrix $\mathbf{k}_e$ for each element is defined as

$$\mathbf{k}_e = \mathbf{k}_b + \mathbf{k}_s + \mathbf{k}_m \tag{22}$$

where $\mathbf{k}_b$, $\mathbf{k}_s$ and $\mathbf{k}_m$ represent the bending, shear, and axial stiffness matrices of the element, respectively, and they can be specified as

$$\mathbf{k}_b = h_e^3 \cdot \int_{\Omega_e} \frac{1}{12} \cdot \mathbf{B}_b^T \mathbf{D}_b \mathbf{B}_b \, \mathrm{d}\boldsymbol{x} = h_e^3 \cdot \mathbf{k}_1 \tag{23}$$

$$\mathbf{k}_s = h_e \cdot \int_{\Omega_e} \mathbf{B}_s^T \mathbf{D}_s \mathbf{B}_s \, \mathrm{d}\boldsymbol{x} = h_e \cdot \mathbf{k}_2 \tag{24}$$

$$\mathbf{k}_m = h_e \cdot \int_{\Omega_e} \mathbf{B}_m^T \mathbf{D}_m \mathbf{B}_m \, \mathrm{d}\boldsymbol{x} = h_e \cdot \mathbf{k}_3 \tag{25}$$

where $\mathbf{B}_b$, $\mathbf{B}_s$ and $\mathbf{B}_m$ are the strain-displacement matrices for bending, shearing, and axial deformation, respectively; $\mathbf{D}_b$, $\mathbf{D}_s$ and $\mathbf{D}_m$ are the corresponding elastic matrices. Ω_e represents the element domain. The stiffness matrix of finite element in Equation (22) can be modified to

$$\mathbf{k}_e = h_e^3 \mathbf{k}_1 + h_e(\mathbf{k}_2 + \mathbf{k}_3) \tag{26}$$

The geometric stiffness matrix is defined as

$$\mathbf{g}_e = \int_{\Omega_e} \mathbf{g}^T \begin{bmatrix} -\sigma_x & -\tau_{xy} \\ -\tau_{xy} & -\sigma_y \end{bmatrix} \mathbf{g} \, h_e \mathrm{d}\boldsymbol{x} \tag{27}$$

where $\mathbf{g}$ represents the partial derivative of the shape functions, and σ_x, σ_y, and τ_{xy} are the plane axial and shear stresses. The expression for $\mathbf{g}_e$ in Equation (27) can be modified to

$$\mathbf{g}_e = h_e \mathbf{g}_1 \tag{28}$$

where $\mathbf{g}_1$ depicts the geometric stiffness matrix of unit thickness.

4.3. Sensitivity Analysis

The sensitivity of the optimization objective J with respect to the design variables α_i is given by

$$\frac{\partial J}{\partial \alpha_i} = -\frac{\partial \lambda_1}{\partial \alpha_i} \tag{29}$$

From Equation (21), the partial derivative of the critical BLF λ_1 with respect to α_i can be acquired as (likewise, the partial derivative of λ_1 regarding the design variables β_i can be derived)

$$\frac{\partial \lambda_1}{\partial \alpha_i} = \frac{1}{\boldsymbol{\varphi}_1^T \mathbf{G} \boldsymbol{\varphi}_1} \left(\sum_{e=1}^{n} \boldsymbol{\varphi}_{1e}^T \frac{\partial \mathbf{k}_e}{\partial \alpha_i} \boldsymbol{\varphi}_{1e} - \lambda_1 \sum_{e=1}^{n} \boldsymbol{\varphi}_{1e}^T \frac{\partial \mathbf{g}_e}{\partial \alpha_i} \boldsymbol{\varphi}_{1e} \right) \tag{30}$$

From Equations (26) and (28), we have

$$\frac{\partial \mathbf{k}_e}{\partial \alpha_i} = \frac{\partial h_e}{\partial \alpha_i} \left(3h_e^2 \mathbf{k}_1 + \mathbf{k}_2 + \mathbf{k}_3 \right) \tag{31}$$

$$\frac{\partial \mathbf{g}_e}{\partial \alpha_i} = \frac{\partial h_e}{\partial \alpha_i} \mathbf{g}_1 \tag{32}$$

Based on Equations (1)–(6) and Equations (8) and (9), we have

$$\frac{\partial h_e}{\partial \alpha_i} = \frac{\partial h_e}{\partial \tilde{\rho}_e} \frac{\partial \tilde{\rho}_e}{\partial \rho_e} \frac{\partial \rho_e}{\partial \Gamma_e} \frac{\partial \Gamma_e}{\partial \gamma_e} \frac{\partial \gamma_e}{\partial \alpha_i} \tag{33}$$

where

$$\frac{\partial h_e}{\partial \tilde{\rho}_e} = h_s \tag{34}$$

$$\frac{\partial \tilde{\rho}_e}{\partial \rho_e} = \frac{\tau \operatorname{sech}^2[\tau(\rho_e - \eta)]}{\tanh(\tau\eta) + \tanh[\tau(1-\eta)]} \tag{35}$$

$$\frac{\partial \rho_e}{\partial \Gamma_e} = \frac{1}{2} + \frac{\Gamma_e - \Theta_e}{2\sqrt{(\Gamma_e - \Theta_e)^2 + \chi}} \tag{36}$$

$$\frac{\partial \Gamma_e}{\partial \gamma_e} = -\frac{\pi}{\mu_1} \sin\left(\frac{2\pi}{\mu_1}\gamma_e\right) \tag{37}$$

$$\frac{\partial \gamma_e}{\partial \alpha_i} = \varphi(\boldsymbol{x}_e, \boldsymbol{q}_i) \tag{38}$$

Next, the sensitivity of the optimization objective J with respect to the design variable η is formulated as

$$\frac{\partial J}{\partial \eta} = -\frac{\partial \lambda_1}{\partial \eta} \tag{39}$$

$$\frac{\partial \lambda_1}{\partial \eta} = \frac{1}{\boldsymbol{\varphi}_1^T \mathbf{G} \boldsymbol{\varphi}_1} \left(\sum_{e=1}^{n} \boldsymbol{\varphi}_{1e}^T \frac{\partial \mathbf{k}_e}{\partial \eta} \boldsymbol{\varphi}_{1e} - \lambda_1 \sum_{e=1}^{n} \boldsymbol{\varphi}_{1e}^T \frac{\partial \mathbf{g}_e}{\partial \eta} \boldsymbol{\varphi}_{1e} \right) \tag{40}$$

Similarly, based on Equations (26) and (28), we have

$$\frac{\partial \mathbf{k}_e}{\partial \eta} = \frac{\partial h_e}{\partial \eta} \left(3h_e^2 \mathbf{k}_1 + \mathbf{k}_2 + \mathbf{k}_3 \right) \tag{41}$$

$$\frac{\partial \mathbf{g}_e}{\partial \eta} = \frac{\partial h_e}{\partial \eta} \mathbf{g}_1 \tag{42}$$

According to Equations (1) and (2), we have

$$\frac{\partial h_e}{\partial \eta} = \frac{\partial h_e}{\partial \tilde{\rho}_e} \frac{\partial \tilde{\rho}_e}{\partial \eta} \tag{43}$$

where

$$\frac{\partial \tilde{\rho}_e}{\partial \eta} = \frac{\tau((Q' - L')(Q + R) - (Q' - R')(Q + L))}{(Q + R)^2} \tag{44}$$

where

$$Q = \tanh(\tau\eta), \quad L = \tanh[\tau(\rho_e - \eta)], \quad R = \tanh[\tau(1 - \eta)] \tag{45}$$

$$Q' = 1 - Q^2, \quad L' = 1 - L^2, \quad R' = 1 - R^2 \tag{46}$$

In accordance with Equation (13), the sensitivity of the volume constraint to α_i, β_i, and η are

$$\frac{\partial V}{\partial \alpha_i} = \sum_{e=1}^{n} \frac{\partial \tilde{\rho}_e}{\partial \rho_e} \frac{\partial \rho_e}{\partial \Gamma_e} \frac{\partial \Gamma_e}{\partial \gamma_e} \frac{\partial \gamma_e}{\partial \alpha_i} h_s A_e \tag{47}$$

$$\frac{\partial V}{\partial \beta_i} = \sum_{e=1}^{n} \frac{\partial \tilde{\rho}_e}{\partial \rho_e} \frac{\partial \rho_e}{\partial \Gamma_e} \frac{\partial \Gamma_e}{\partial \gamma_e} \frac{\partial \gamma_e}{\partial \beta_i} h_s A_e \tag{48}$$

$$\frac{\partial V}{\partial \eta} = \sum_{e=1}^{n} \frac{\partial \tilde{\rho}_e}{\partial \eta} h_s A_e \tag{49}$$

Based on Equation (19), the sensitivity of the gradient constraint g_γ to α_i is

$$\frac{\partial g_\gamma}{\partial \alpha_i} = g_\gamma^{(1-p_2)} \sum_{e=1}^{n} \left(d_e^\gamma\right)^{(p_2-1)} \frac{\partial d_e^\gamma}{\partial \alpha_i} \tag{50}$$

According to Equations (14)–(17), we have

$$\frac{\partial d_e^\gamma}{\partial \alpha_i} = 2\left(1 - \frac{1}{\|\nabla \gamma\|}\right)\left[\left(\sum_{j=1}^{m} \alpha_j \frac{\partial \varphi_j}{\partial x}\right)\frac{\partial \varphi_i}{\partial x} + \left(\sum_{j=1}^{m} \alpha_j \frac{\partial \varphi_j}{\partial y}\right)\frac{\partial \varphi_i}{\partial y}\right] \tag{51}$$

Under the same conditions, the sensitivity of the gradient constraint g_θ concerning the design variables β_i can be acquired. All design variables are updated by using the method of move asymptote (MMA) [47].

5. Numerical Examples

In this part, several numerical examples of optimizing the fundamental BLF for the structures with grid stiffeners are provided. For all examples, the Young's modulus is set to 200 GPa, the Poisson's ratio is set to 0.3, the thickness of the base plate h_b is 0.5 mm, and the thickness of the stiffener h_s is 1 mm. The parameter τ in Equation (2) is set to 7, the parameter p_2 in Equations (19) and (20) is 12, the support radius parameter d_s of CS-RBF is set to 8, and the maximum and minimum limits for the design variables in optimization problem are set as follows: $\alpha_{\min} = -50$, $\alpha_{\max} = 50$, $\beta_{\min} = -50$, $\beta_{\max} = 50$, $\eta_{\min} = 0$, $\eta_{\max} = 2$.

The convergence condition for optimization is characterized as

$$E_{err} = \frac{\left|\sum_{f=1}^{5}\left|E^{k-f+1} - E^{k-5-f+1}\right|\right|}{\sum_{f=1}^{5} E^{k-f+1}} \le \delta_E \tag{52}$$

where E_{err} represents the error between the relevant objective functions during the optimization process; k indicates the current iteration step; δ_E is the upper limit of the error, and it is set to 0.2%. Additionally, if the iteration step k reaches 600, the optimization procedure will be terminated.

5.1. Example 1

Within this example, a square plate with dimensions of 10 mm × 10 mm, supported on both sides with simply supported boundary conditions, is considered. Uniform compressive loads of magnitude $F = 1$ N/mm are applied simultaneously on both sides. The boundary conditions are illustrated in Figure 7: the bottom-left corner of the plate is restricted in the x and y-direction translational degrees of freedom (i.e., $u = 0$ and $v = 0$), the translational degree of freedom in the y-direction at the bottom-right corner is constrained, and the z-direction degrees of freedom on all four sides of the plate are fixed (i.e., $w = 0$). The wavelength parameters in Equations (5) and (6) are set to $\mu_1 = \mu_2 = 1.4$. The design domain consists of 200 × 200 finite element elements, with 20 × 20 CS-RBF knots distributed uniformly within the design domain. To maintain uniformity in the width of the stiffeners post-optimization, the parameter ξ in Equations (19) and (20) is set to 0.3.

Several upper bounds of volume are applied in this example, and the stiffeners of the initial design are set in two directions: horizontal (0°) and vertical (90°), as shown in Figure 8a. In Equation (13), the volume constraints for stiffeners are defined as $\overline{V} = 0.8V^0$, $\overline{V} = V^0$, and $\overline{V} = 1.2V^0$, respectively, where V^0 is the initial volume of the stiffeners. The optimization results are illustrated in Figure 8b–d.

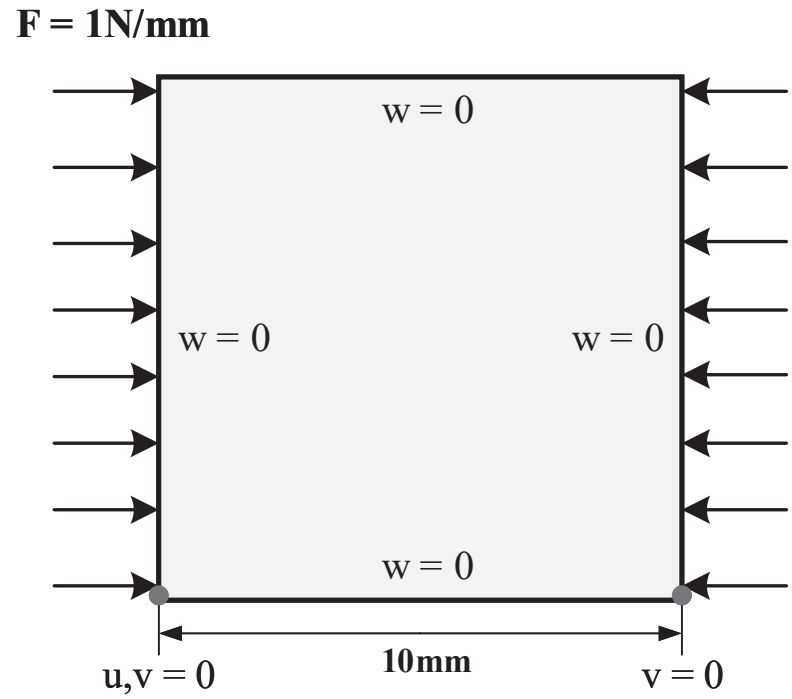

Figure 7. The design domain and boundary conditions for Example 1.

It can be seen that despite varying volume constraints on the stiffeners, the layout of the stiffeners remains essentially consistent. The effect of volume constraint manifests in the width of the stiffeners, where a larger volume leads to wider stiffeners. Regarding the layout, it is notable that the distance between stiffeners increases in the central region. This enhances the structural strength in the central region. The path of the stiffeners forms outwardly curved arcs, aiming to enhance the load-bearing capacity against axial compression loads on both sides. Figure 9a–c depict the corresponding first buckling modes of the three optimized structures, and it should be noted that the buckling mode in this example, as well as in all subsequent examples, represents the structure's normalized displacement in the w-direction.

Figure 10a–c depict the first two BLFs and volume variation curves under three different volume constraint scenarios. It is apparent that there is no intersection between the curves of the first and second BLFs, indicating the absence of repeated first BLFs. Additionally, the volume changes for each case follow the prescribed volume constraint values, eventually reaching their respective maximum allowable volume. Furthermore, it can be seen that the optimization of the critical BLF converges under all three constraint conditions, demonstrating the validity of the optimization.

Table 1 presents the corresponding outcomes of the optimization, indicating a clear trend where increasing volume leads to higher buckling load. Under the maximum allowable volumes of 1 times and 1.2 times the initial volume, the increment in critical buckling load reaches 13.3% and 44.5%, respectively. When $\overline{V} = 0.8V^0$, the buckling load decreases on account of the reduced volume of the stiffeners.

Table 1. Comparison of results under divergent volume constraints (λ_1^0, V^0: initial critical BLF and total volume of stiffeners; $\lambda_1^\#$, $V^\#$: final critical BLF and total volume of stiffeners; $\Delta\lambda_1 = \lambda_1^\# - \lambda_1^0$; $V^0 = 50.55$ and $\lambda_1^0 = 5586.5$).

$\overline{V}$	$\lambda_1^\#$	$V^\#$	$V^\#/V^0$	$\Delta\lambda_1/\lambda_1^0$
$0.8V^0$	4916.3	40.44	80.00%	−12.0%
V^0	6330.8	50.54	99.98%	13.3%
$1.2V^0$	8070.1	60.64	119.96%	44.5%

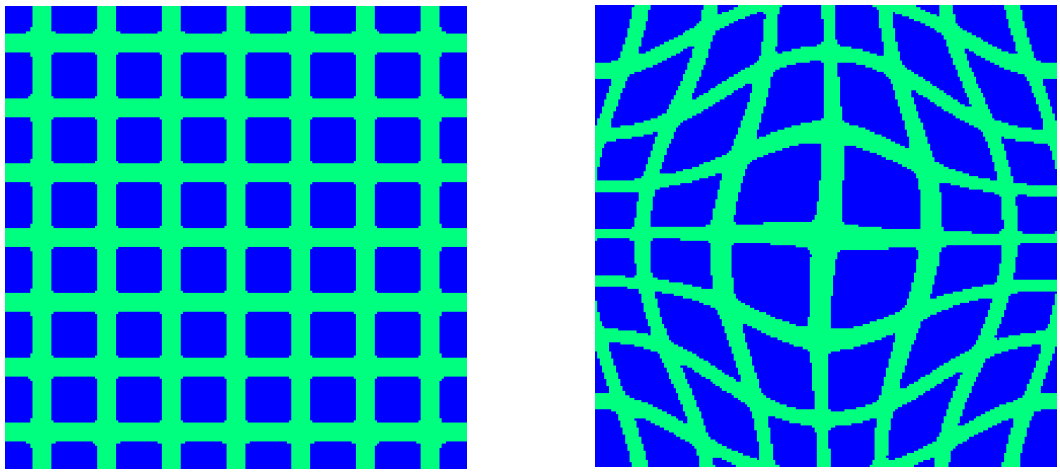

(**a**) initial design (**b**) optimized with $\overline{V} = 0.8V^0$

(**c**) optimized with $\overline{V} = V^0$ (**d**) optimized with $\overline{V} = 1.2V^0$

Figure 8. Optimization results under different volume constraints on stiffeners. (**a**) Initial design, (**b**) optimized design under volume constraint $\overline{V} = 0.8V^0$, (**c**) optimized design under volume constraint $\overline{V} = V^0$, and (**d**) optimization results under volume constraint $\overline{V} = 1.2V^0$.

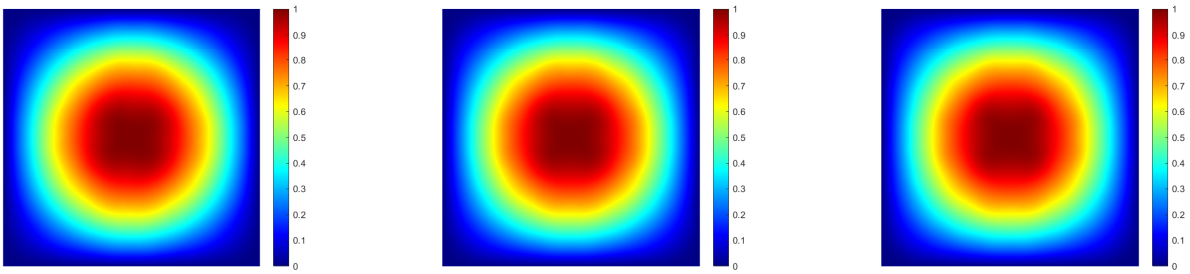

(**a**) $\lambda_1 = 4916.3$ (**b**) $\lambda_1 = 6330.8$ (**c**) $\lambda_1 = 8070.1$

Figure 9. First-order buckling mode of the grid stiffener structure optimized under different volume constraint conditions, (**a**) volume constraint $\overline{V} = 0.8V^0$, (**b**) volume constraint $\overline{V} = V^0$, and (**c**) volume constraint $\overline{V} = 1.2V^0$.

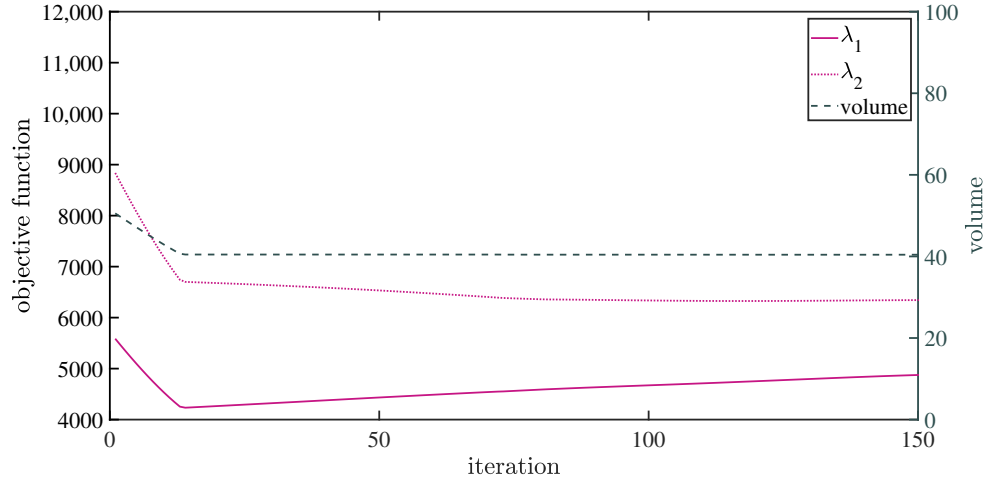

(**a**) volume constraint $\overline{V} = 0.8V^0$

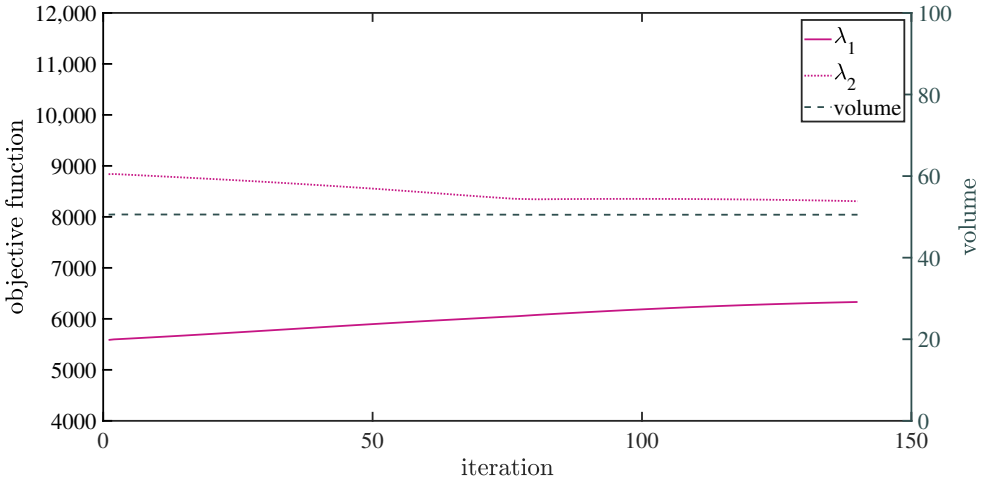

(**b**) volume constraint $\overline{V} = V^0$

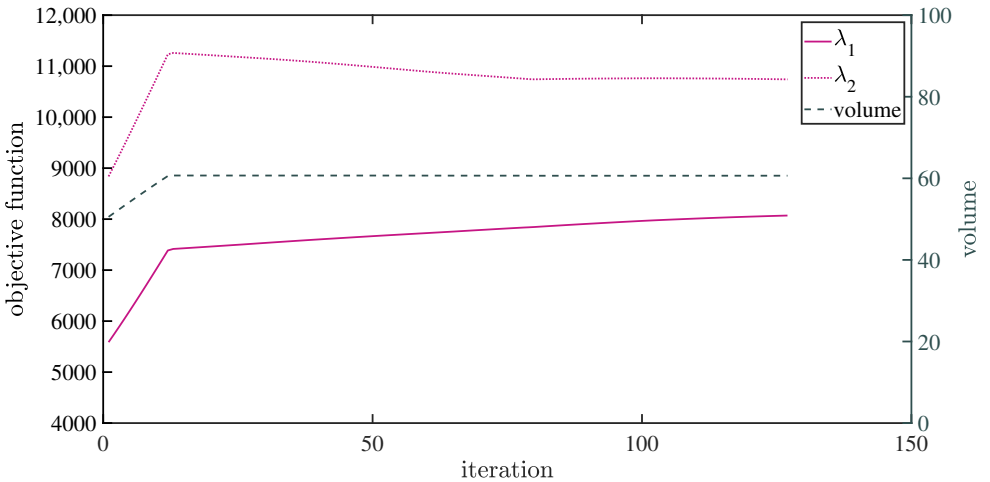

(**c**) volume constraint $\overline{V} = 1.2V^0$

Figure 10. History of the first two buckling load factors (BLFs) and stiffeners volume under different volume constraints (λ_1 and λ_2 symbolize the first and second BLFs, respectively).

5.2. Example 2

In this case, the size of the design domain is the same as that in Example 1, with the left end fixed and a uniform compressive load of magnitude $F = 1$ N/mm applied on the right side, as shown in Figure 11. The wavelength parameters in Equations (5) and (6), as

well as the finite element mesh division and the distribution of CS-RBF nodes, are the same as those in Example 1. The maximum allowable volume $\overline{V}$ is configured as V^0.

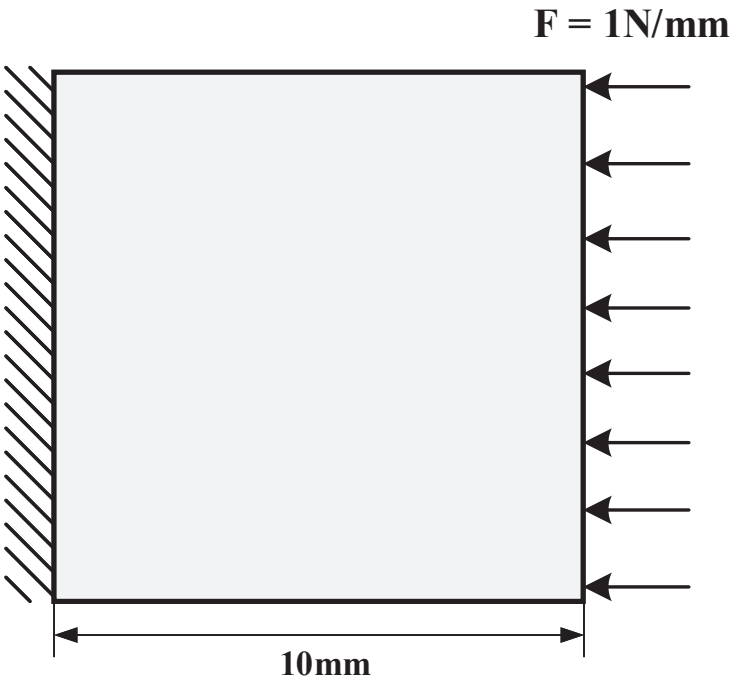

Figure 11. The design domain and boundary conditions for Example 2.

The initial layout of the stiffeners is in two directions, 45° and −45°, as shown in Figure 12a. Both scenarios with and without gradient constraints are considered. In the case of with gradient constraints, the gradient constraint values in Equations (19) and (20) are set to $\xi = 0.06$ and $\xi = 0.3$, respectively. The optimization results are illustrated in Figure 12b–d. It is clear that the optimization results with gradient constraints have more uniform width of the stiffeners. Moreover, the stricter the gradient constraint, the more pronounced this effect. Regarding the stiffener layout, it is evident that the stiffeners on the left side are optimized to align with the direction of force transmission (horizontal direction in the figure), with increased width, thereby enhancing the ability to withstand axial compressive loads more effectively. Figure 13a–c, respectively, depict the first buckling modes under gradient constraints of $\xi = 0.06$, $\xi = 0.3$, and without gradient constraints.

Figure 14 illustrates the variation of gradients of the level set functions during the optimization process. Figure 14a–c, respectively, represent the cases with gradient constraints $\xi = 0.06$, $\xi = 0.3$, and without gradient constraints. One can see that under the gradient constraint conditions, the gradients eventually reach the set values, satisfying the gradient constraint requirements. In the absence of gradient constraints, the gradient values are ultimately optimized to 0.54.

In Figure 15, the history of the objective function and volume are displayed under three different cases. It can be observed that the volume remains close to a constant value throughout, validating the effectiveness of the volume constraint. The optimization magnitude of the critical BLF increases as the gradient constraint weakens. Particularly, the optimization magnitude is greatest when there is no gradient constraint. Hence, relaxing the gradient constraint can lead to better performance. In Table 2, it is clear to see the optimization magnitude is 26.1% with a gradient constraint value of $\xi = 0.06$, 45.2% with $\xi = 0.3$, and 47.1% without gradient constraints.

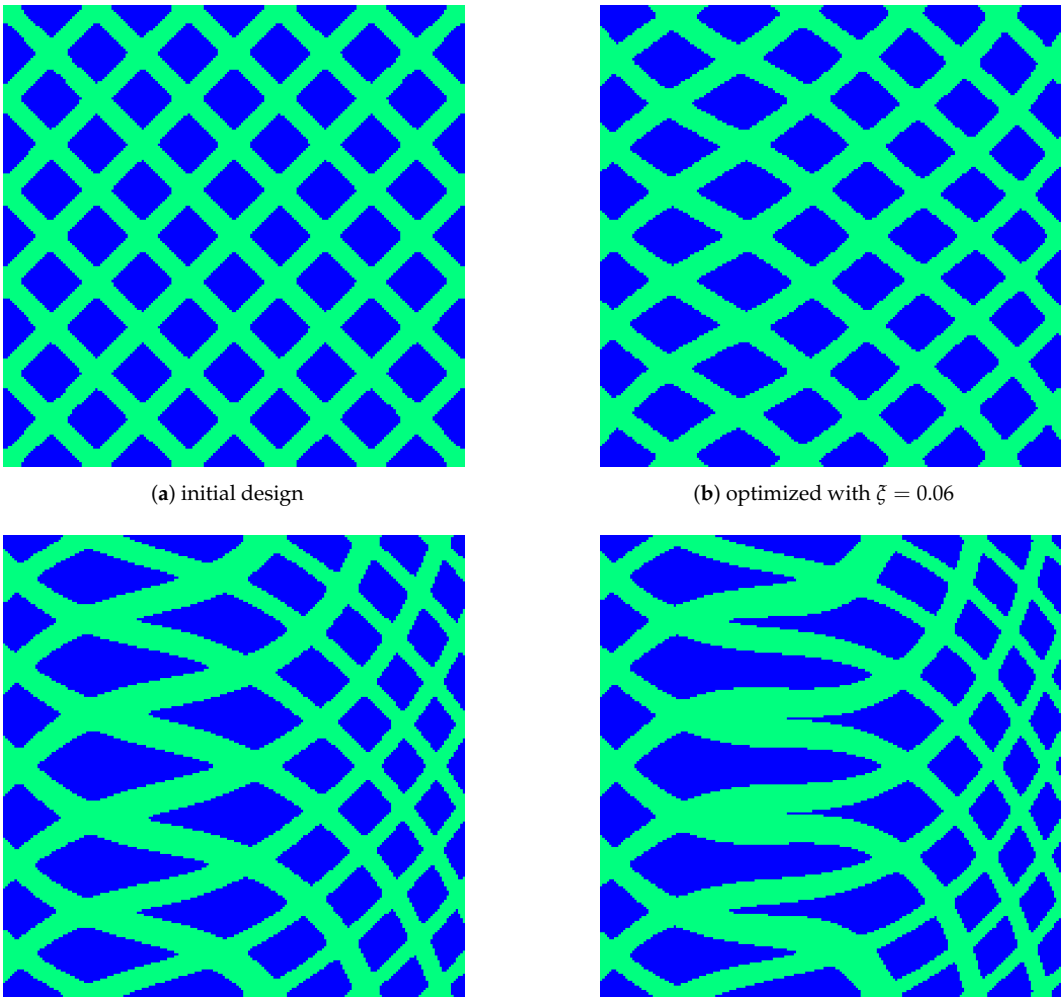

(**a**) initial design (**b**) optimized with $\xi = 0.06$

(**c**) optimized with $\xi = 0.3$ (**d**) optimized without ξ

Figure 12. Results under different gradient constraints. (**a**) Initial design, (**b**) optimization design with gradient constraint $\xi = 0.06$, (**c**) optimization design with gradient constraint $\xi = 0.3$, (**d**) optimization design without gradient constraint.

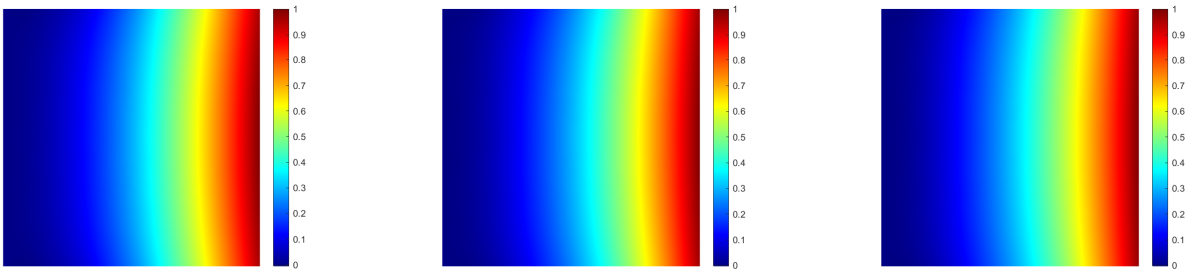

(**a**) $\lambda_1 = 437.89$ (**b**) $\lambda_1 = 503.96$ (**c**) $\lambda_1 = 510.77$

Figure 13. First-order buckling mode of the grid stiffener structure optimized under different gradient constraint conditions, (**a**) gradient constraint $\xi = 0.06$, (**b**) gradient constraint $\xi = 0.3$, and (**c**) without gradient constraint.

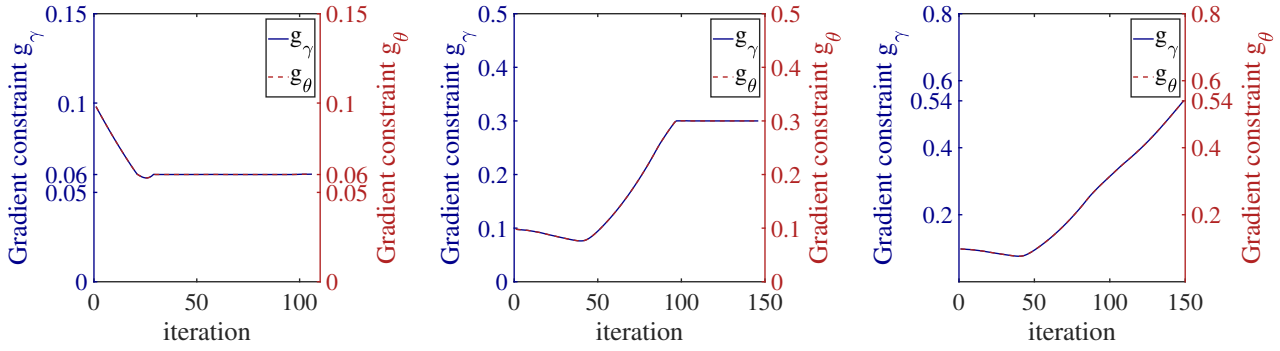

(**a**) optimized with $\xi = 0.06$ (**b**) optimized with $\xi = 0.3$ (**c**) optimized without ξ

Figure 14. Variation of different gradients during optimization processes.

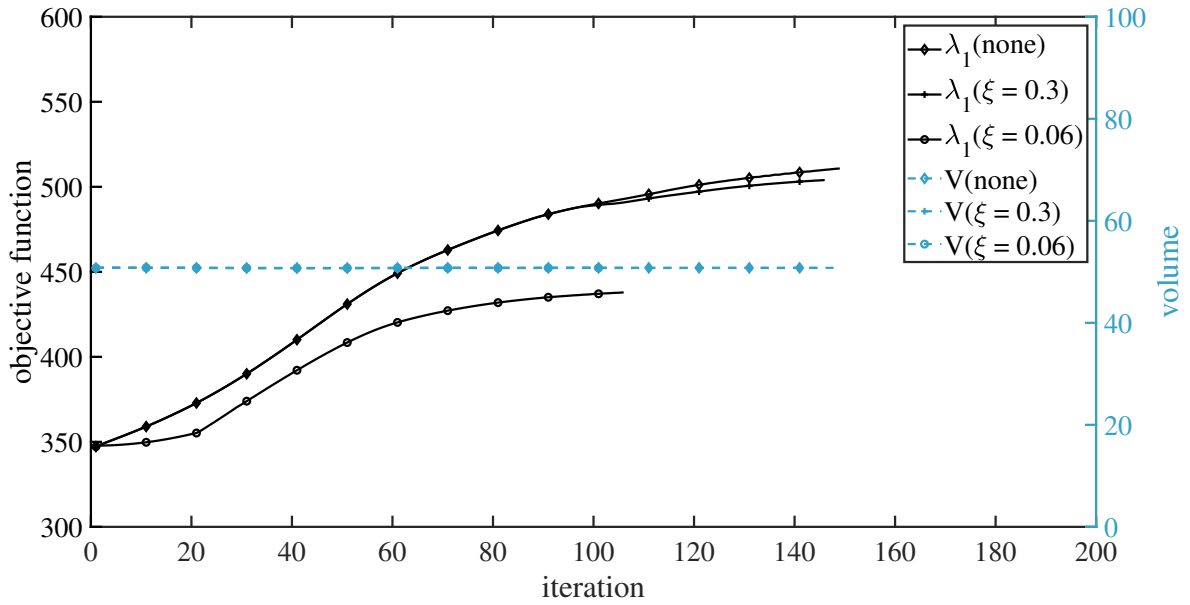

Figure 15. The variations of critical BLF and stiffeners volume under different gradient constraints.

Table 2. Comparison of results under divergent gradient constraints (λ_1^0, V^0: critical BLF and initial total volume of stiffeners; $\lambda_1^\#$, $V^\#$: critical BLF and final total volume of stiffeners; $\Delta\lambda_1 = \lambda_1^\# - \lambda_1^0$; $\lambda_1^0 = 347.20$ and $V^0 = 50.76$).

ξ	$\lambda_1^\#$	$V^\#$	$V^\#/V^0$	$\Delta\lambda_1/\lambda_1^0$
0.06	437.89	50.76	100%	26.1%
0.3	503.96	50.76	100%	45.1%
none	510.77	50.76	100%	47.1%

5.3. Example 3

The design domain of this case study is a rectangular shape with dimensions of 10 mm × 20 mm. The bottom edge is completely fixed, and a vertically downward distributed load is applied on top with a length of 2 mm and a magnitude of $F = 1$ N/mm. Boundary conditions are depicted in Figure 16. The wavelength parameters in Equations (5) and (6) are set to $\mu_1 = \mu_2 = 2.1$; 200 × 400 finite elements is used; and 20 × 40 CS-RBF knots are uniformly distributed. The gradient constraint parameter ξ in Equations (19) and (20) is configured as 0.3. The maximum allowable volume $\overline{V}$ is set to be V^0.

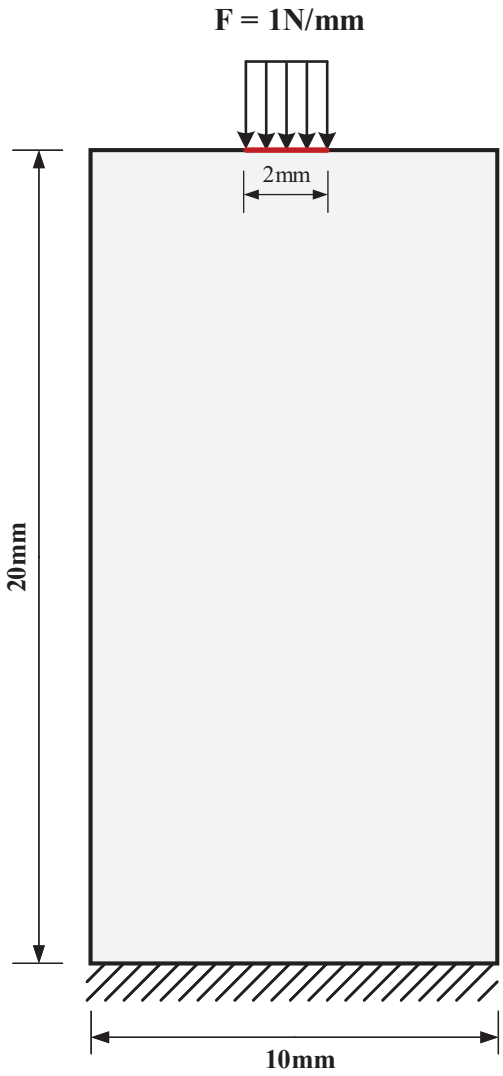

Figure 16. The design domain and boundary conditions for Example 3.

In this example, the initial layout of the stiffeners is oriented in two directions, at 45° and −45°, as illustrated in Figure 17a. Figure 17b exhibits the final outcome, where the stiffeners distribution at the bottom, near the center region, resembles that of Example 2, optimized in the direction of the load path, thereby enhancing the load-bearing capacity. The stiffeners in the upper region follow an arch-shaped path, similarly aimed at improving the load-bearing capacity. Figure 18a–c represents the first-, second-, and third-order buckling modes corresponding to the optimization results, respectively, demonstrating the absence of duplicate first-order BLFs.

The plots depicting the evolution of the critical BLF and the volume of stiffeners are illustrated in Figure 19. The optimization procedure converged eventually, with the critical BLF λ_1 increasing by 29.8%.

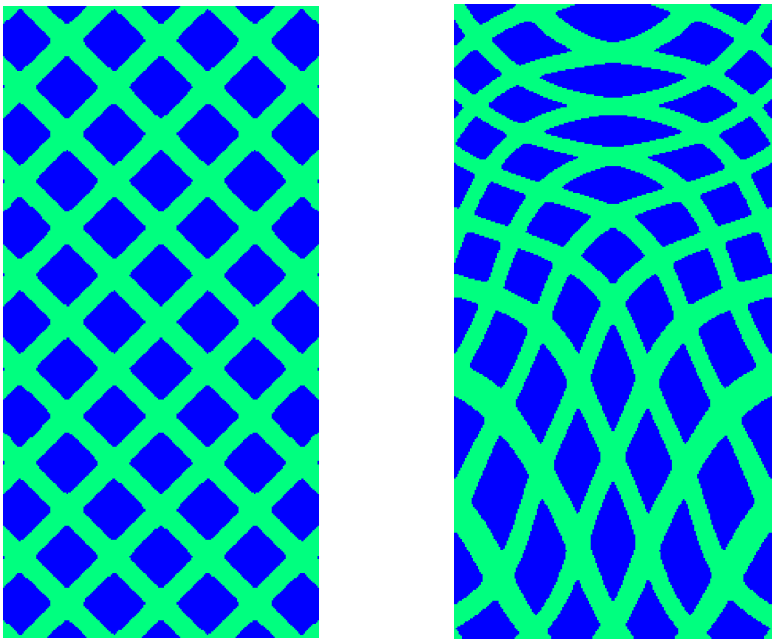

(**a**) initial design (**b**) optimized design

Figure 17. Initial design and optimized result.

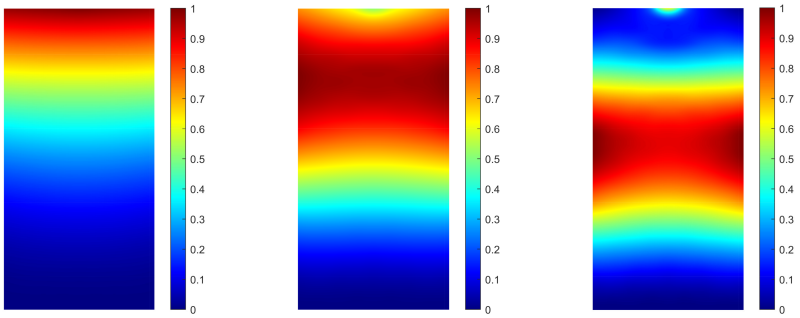

(**a**) $\lambda_1 = 569.94$ (**b**) $\lambda_2 = 3493.5$ (**c**) $\lambda_3 = 7913.8$

Figure 18. Optimization of the first three buckling modes for the grid stiffener structure. (**a**) First buckling mode, (**b**) second buckling mode, (**c**) third buckling mode.

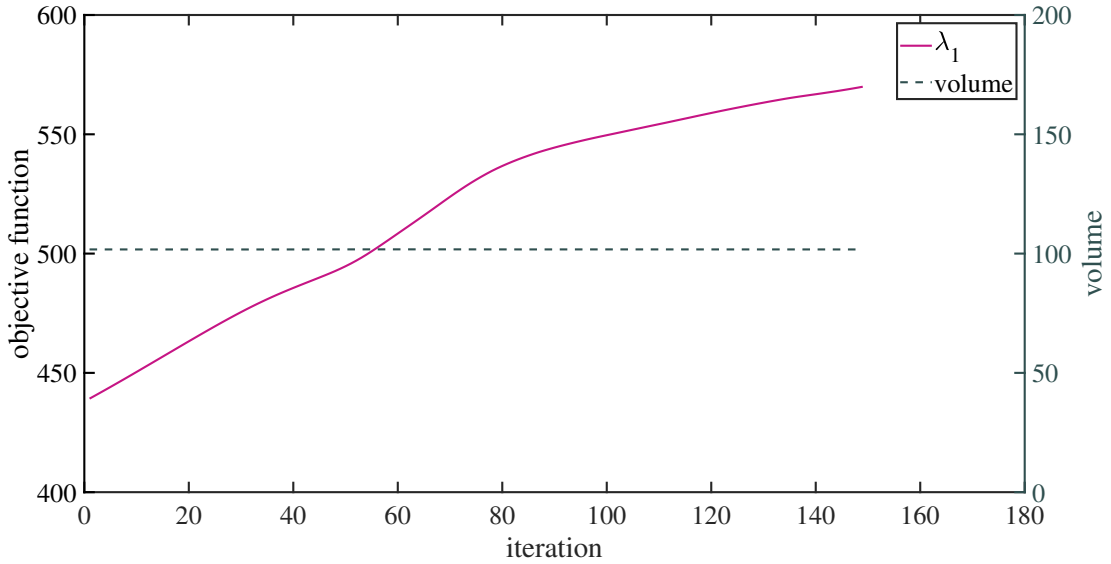

Figure 19. Convergence history of critical BLF and stiffeners volume.

6. Conclusions

In this study, we optimized the critical buckling load of curved grid stiffener structures based on a level-set-based density method. By transforming two fundamental level set functions, two clusters of stiffeners were obtained, and the real density of each element was obtained using density-based methods. Then, the overall structural element height distribution was obtained by adding the heights of the matrix and stiffeners. The Mindlin plate theory was used for finite element analysis of buckling, and the stiffness matrix and geometric stiffness matrix of each element were determined and assembled into the overall matrix. After that, the eigenvalue equation was solved to obtain the corresponding eigenvalues and eigenvectors. Combining this with the optimization objective, relevant sensitivity analysis calculations were performed. Simultaneously, volume and gradient constraints were added to improve material utilization and maintain uniform stiffeners width. Finally, the MMA algorithm was used to update the design variables. The effectiveness of the proposed method was validated through several numerical examples.

In practical applications, this research method improves the stability of grid stiffener structures under specific load conditions in engineering applications. Optimizing the stiffener layout instead of increasing the stiffener thickness or base wall thickness helps the structure move towards lightweight development. In addition, introducing gradient constraints to control the minimum spacing between stiffeners enhances the manufacturability of the structure. In the future, the layout and shape of the obtained grid stiffener structure can be subjected to certain post-processing to meet further requirements, and specific experimental analysis can be added for verification and explanation. In addition, the method can be combined with topology optimization to change the shape of base structure while optimizing the layout of curved grid stiffeners.

Author Contributions: Conceptualization, Y.Z. and Q.X.; methodology, Y.Z.; validation, Y.Z.; formal analysis, Y.Z.; writing—original draft preparation, Y.Z.; writing—review and editing, Q.X. and Y.T.; supervision, Q.X. All authors have read and agreed to the published version of the manuscript.

Funding: This research was funded by National Natural Science Foundation of China, grant number 12272144.

Institutional Review Board Statement: Not applicable.

Informed Consent Statement: Not applicable.

Data Availability Statement: The data used to support the findings of this study are available within the article.

Acknowledgments: The authors also gratefully thank Krister Svanberg for providing the MMA codes.

Conflicts of Interest: The authors declare no conflicts of interest.

References

1. Jadhav, P.; Mantena, P.R. Parametric optimization of grid-stiffened composite panels for maximizing their performance under transverse loading. *Compos. Struct.* **2007**, *77*, 353–363. [CrossRef]
2. Wang, B.; Tian, K.; Hao, P.; Cai, Y.; Li, Y.; Sun, Y. Hybrid analysis and optimization of hierarchical stiffened plates based on asymptotic homogenization method. *Compos. Struct.* **2015**, *132*, 136–147. [CrossRef]
3. Zhu, J.H.; Zhang, W.H.; Xia, L. Topology Optimization in Aircraft and Aerospace Structures Design. *Arch. Comput. Method Eng.* **2016**, *23*, 595–622. [CrossRef]
4. Kapania, R.; Li, J.; Kapoor, H. Optimal design of unitized panels with curvilinear stiffeners. In Proceedings of the AIAA 5th ATIO and16th Lighter-Than-Air Sys Tech. and Balloon Systems Conferences, Arlington, VA, USA, 26–28 September 2005 ; p. 7482.
5. Paschero, M.; Hyer, M.W. Improvement of Axial Buckling Capacity of Elliptical Lattice Cylinders. *AIAA J.* **2011**, *49*, 396–410. [CrossRef]
6. Totaro, G.; De Nicola, F. Recent advance on design and manufacturing of composite anisogrid structures for space launchers. *Acta Astronaut.* **2012**, *81*, 570–577. [CrossRef]
7. Hao, P.; Wang, B.; Tian, K.; Li, G.; Du, K.; Niu, F. Efficient Optimization of Cylindrical Stiffened Shells with Reinforced Cutouts by Curvilinear Stiffeners. *AIAA J.* **2016**, *54*, 1350–1363. [CrossRef]

8. Zhao, W.; Kapania, R.K. Buckling analysis of unitized curvilinearly stiffened composite panels. *Compos. Struct.* **2016**, *135*, 365–382. [CrossRef]
9. Gil-Ureta, F.; Pietroni, N.; Zorin, D. Reinforcement of General Shell Structures. *ACM Trans. Graph.* **2020**, *39*, 1–19. [CrossRef]
10. Laccone, F.; Pietroni, N.; Cignoni, P.; Malomo, L. Bending-Reinforced Grid Shells for Free-form Architectural Surfaces. *Comput.-Aided Des.* **2024**, *168*, 103670. [CrossRef]
11. Mulani, S.; Locatelli, D.; Kapania, R. Grid-stiffened panel optimization using curvilinear stiffeners. In Proceedings of the 52nd AIAA/ASME/ASCE/AHS/ASC Structures, Structural Dynamics and Materials Conference 19th AIAA/ASME/AHS Adaptive Structures Conference 13t, Denver, CO, USA, 4–7 April 2011; p. 1895.
12. Mulani, S.B.; Slemp, W.C.H.; Kapania, R.K. EBF3PanelOpt: An optimization framework for curvilinear blade-stiffened panels. *Thin-Walled Struct.* **2013**, *63*, 13–26. [CrossRef]
13. Wang, D.; Abdalla, M.M.; Zhang, W. Buckling optimization design of curved stiffeners for grid-stiffened composite structures. *Compos. Struct.* **2017**, *159*, 656–666. [CrossRef]
14. Wang, D.; Abdalla, M.M.; Wang, Z.P.; Su, Z. Streamline stiffener path optimization (SSPO) for embedded stiffener layout design of non-uniform curved grid-stiffened composite (NCGC) structures. *Comput. Meth. Appl. Mech. Eng.* **2019**, *344*, 1021–1050. [CrossRef]
15. Yang, K.; Tian, Y.; Shi, T.; Xia, Q. A Level Set Based Density Method for Optimizing Structures with Curved Grid Stiffeners. *Comput.-Aided Des.* **2022**, *153*, 103407. [CrossRef]
16. Bostan, B.; Kusbeci, M.; Cetin, M.; Kirca, M. Buckling performance of fuselage panels reinforced with Voronoi-type stiffeners. *Int. J. Mech. Sci.* **2023**, *240*, 107923. [CrossRef]
17. Cai, J.; Moen, C.D. Elastic buckling analysis of thin-walled structural members with rectangular holes using generalized beam theory. *Thin-Walled Struct.* **2016**, *107*, 274–286. [CrossRef]
18. Ferrari, F.; Sigmund, O.; Guest, J.K. Topology optimization with linearized buckling criteria in 250 lines of Matlab. *Struct. Multidiscip. Optim.* **2021**, *63*, 3045–3066. [CrossRef]
19. Xu, T.; Huang, X.; Lin, X.; Xie, Y.M. Topology optimization for maximizing buckling strength using a linear material model. *Comput. Meth. Appl. Mech. Eng.* **2023**, *417*, 107923. [CrossRef]
20. Falkowicz, K. Experimental and numerical analysis of compression thin-walled composite plates weakened by cut-outs. *Arch. Civ. Eng.* **2017**, *63*, 161–172. [CrossRef]
21. Falkowicz, K.; Debski, H.; Teter, A. Design solutions for improving the lowest buckling loads of a thin laminate plate with notch. In AIP Conference Proceedings, Proceedings of the 22nd International Conference on Computer Methods in Mechanics, Lublin, Poland, 13–16 September 2017; AIP Publishing: Melville, NY, USA, 2017; Volume 1922.
22. Falkowicz, K. Stability and Failure of Thin-Walled Composite Plate Elements with Asymmetric Configurations. *Materials* **2024**, *17*, 1943. [CrossRef]
23. Wang, D.; Abdalla, M.M.; Zhang, W. Sensitivity analysis for optimization design of non-uniform curved grid-stiffened composite (NCGC) structures. *Compos. Struct.* **2018**, *193*, 224–236. [CrossRef]
24. Shi, P.; Kapania, R.K.; Dong, C.Y. Vibration and Buckling Analysis of Curvilinearly Stiffened Plates Using Finite Element Method. *AIAA J.* **2015**, *53*, 1319–1335. [CrossRef]
25. Hao, P.; Wang, B.; Li, G.; Meng, Z.; Tian, K.; Tang, X. Hybrid optimization of hierarchical stiffened shells based on smeared stiffener method and finite element method. *Thin-Walled Struct.* **2014**, *82*, 46–54. [CrossRef]
26. Wang, B.; Hao, P.; Li, G.; Tian, K.; Du, K.; Wang, X.; Zhang, X.; Tang, X. Two-stage size-layout optimization of axially compressed stiffened panels. *Struct. Multidiscip. Optim.* **2014**, *50*, 313–327. [CrossRef]
27. Luo, Y.; Zhan, J. Linear buckling topology optimization of reinforced thin-walled structures considering uncertain geometrical imperfections. *Struct. Multidiscip. Optim.* **2020**, *62*, 3367–3382. [CrossRef]
28. Wang, D.; Abdalla, M.M. Global and local buckling analysis of grid-stiffened composite panels. *Compos. Struct.* **2015**, *119*, 767–776. [CrossRef]
29. Wang, D.; Yeo, S.Y.; Su, Z.; Wang, Z.P.; Abdalla, M.M. Data-driven streamline stiffener path optimization (SSPO) for sparse stiffener layout design of non-uniform curved grid-stiffened composite (NCGC) structures. *Comput. Meth. Appl. Mech. Eng.* **2020**, *365*, 113001. [CrossRef]
30. Zheng, Q.; Jiang, D.; Huang, C.; Shang, X.; Ju, S. Analysis of failure loads and optimal design of composite lattice cylinder under axial compression. *Compos. Struct.* **2015**, *131*, 885–894. [CrossRef]
31. Singh, K.; Kapania, R.K. Accelerated optimization of curvilinearly stiffened panels using deep learning. *Thin-Walled Struct.* **2021**, *161*, 107418. [CrossRef]
32. Wang, F.; Lazarov, B.S.; Sigmund, O. On projection methods, convergence and robust formulations in topology optimization. *Struct. Multidiscip. Optim.* **2010**, *43*, 767–784. [CrossRef]
33. Groen, J.P.; Sigmund, O. Homogenization-based topology optimization for high-resolution manufacturable microstructures. *Int. J. Numer. Methods Eng.* **2017**, *113*, 1148–1163. [CrossRef]
34. Wang, S.; Wang, M.Y. Radial basis functions and level set method for structural topology optimization. *Int. J. Numer. Methods Eng.* **2006**, *65*, 2060–2090. [CrossRef]
35. Luo, Z.; Tong, L.; Wang, M.Y.; Wang, S. Shape and topology optimization of compliant mechanisms using a parameterization level set method. *J. Comput. Phys.* **2007**, *227*, 680–705. [CrossRef]

36. Wang, Y.; Luo, Z.; Kang, Z.; Zhang, N. A multi-material level set-based topology and shape optimization method. *Comput. Meth. Appl. Mech. Eng.* **2015**, *283*, 1570–1586. [CrossRef]
37. Wei, P.; Li, Z.; Li, X.; Wang, M.Y. An 88-line MATLAB code for the parameterized level set method based topology optimization using radial basis functions. *Struct. Multidiscip. Optim.* **2018**, *58*, 831–849. [CrossRef]
38. Shi, S.; Zhou, P.; Lü, Z. A density-based topology optimization method using radial basis function and its design variable reduction. *Struct. Multidiscip. Optim.* **2021**, *64*, 2149–2163. [CrossRef]
39. Jiang, L.; Chen, S. Parametric structural shape & topology optimization with a variational distance-regularized level set method. *Comput. Meth. Appl. Mech. Eng.* **2017**, *321*, 316–336. [CrossRef]
40. Fernandez, F.; Compel, W.S.; Lewicki, J.P.; Tortorelli, D.A. Optimal design of fiber reinforced composite structures and their direct ink write fabrication. *Comput. Meth. Appl. Mech. Eng.* **2019**, *353*, 277–307. [CrossRef]
41. Tian, Y.; Shi, T.; Xia, Q. Buckling optimization of curvilinear fiber-reinforced composite structures using a parametric level set method. *Front. Mech. Eng.* **2024**, *19*, 9. [CrossRef]
42. Le, C.; Norato, J.; Bruns, T.; Ha, C.; Tortorelli, D. Stress-based topology optimization for continua. *Struct. Multidiscip. Optim.* **2009**, *41*, 605–620. [CrossRef]
43. Hughes, T.J.; Tezduyar, T. Finite elements based upon Mindlin plate theory with particular reference to the four-node bilinear isoparametric element. *J. Appl. Mech.* **1981**, *48*, 587–596. [CrossRef]
44. Batista, M. An elementary derivation of basic equations of the Reissner and Mindlin plate theories. *Eng. Struct.* **2010**, *32*, 906–909. [CrossRef]
45. Ma, H.M.; Gao, X.L.; Reddy, J.N. A non-classical Mindlin plate model based on a modified couple stress theory. *Acta Mech.* **2011**, *220*, 217–235. [CrossRef]
46. Liu, H.; Chen, L.; Shi, T.; Xia, Q. M-VCUT level set method for the layout and shape optimization of stiffeners in plate. *Compos. Struct.* **2022**, *293*, 115614. [CrossRef]
47. Svanberg, K. The method of moving asymptotes—a new method for structural optimization. *Int. J. Numer. Methods Eng.* **2005**, *24*, 359–373. [CrossRef]